Wave drag due to generation of capillary-gravity surface waves

Teodor Burghelea and Victor Steinberg

Department of Physics of Complex Systems, The Weizmann Institute of Science, Rehovot 76100, Israel

The onset of the *wave resistance* via the generation of capillary-gravity waves by a small object moving with a velocity V is investigated experimentally. Due to the existence of a minimum phase velocity V_c for surface waves, the problem is similar to the generation of rotons in superfluid helium near their minimum. In both cases, waves or rotons are produced at $V > V_c$ due to *Cherenkov radiation*. We find that the transition to the wave drag state is continuous: in the vicinity of the bifurcation the wave resistance force is proportional to $\sqrt{V - V_c}$ for various fluids. This observation contradicts the theory of Raphaël and de Gennes. We also find that the reduced wave drag force for different fluids and different ball size may be scaled in such a way that all the data collapse on a single curve. The capillary-gravity wave pattern and the shape of the wave-generating region are investigated both experimentally and theoretically. Good agreement between the theory and the experimental data is found in this case.

I. INTRODUCTION

An object, partially submerged in a fluid and moving uniformly on a free fluid surface, is subjected to a drag force that can be of different physical nature. The most common one is a viscous drag, which at low Reynolds numbers, Re ≤ 1, is the Stokes drag, $R_f = 3\pi\eta dV$, that is proportional to the object velocity V. (Here d is the sphere diameter and η is the viscosity.) At higher Re, there is another contribution to the drag, which originates from either laminar or turbulent wakes, called the eddy resistance R_e [1]. However, there exists another contribution to the drag force, R_w, due to the generation of surface capillary-gravity by the uniformly moving object. These waves remove momentum from the object into infinity, and in this way produces the wave resistance force, acting on the object [2].

The problem of the wave resistance for long wavelength gravity waves is rather old one. It was an active subject of research for many years from the end of 19th century in relation to ship navigation and naval architecture. Since the viscosity of water is small, R_f and R_e contributions associated with the viscosity are small compared with the wave resistance exerted on a ship. Thus, in the case of a large object generating the gravity waves, the total drag consists mainly of the wave resistance.

Kelvin was the first to introduce a theoretical model to calculate the wave resistance [4]. Instead of solving a full hydrodynamic problem of a flow past a body of arbitrary shape, he suggested to consider a moving pressure point applied along the body course to a free fluid surface. Later, Kelvin's model was modified into a moving pressure area [5]. So the wave resistance was calculated for a given pressure distribution. Further development brought more sophisticated linear and nonlinear models, which provide a numerical solution of the problem and describe main features of the phenomenon [6]. On the other hand, it seems to be surprising, but, hitherto, nobody noticed that the wave resistance appears due to a bifurcation similar to many other nonequilibrium threshold phenomena, such as Rayleigh-Benard convection, Couette-Taylor flow, etc.

In the case of the gravity waves, Shliomis and Steinberg [7] showed recently that there is a critical velocity V_c such that for $V < V_c$ one finds $R_w = 0$. This critical velocity is defined by the characteristic size of the object, L (e.g., by the ship length), so $V_c = \sqrt{gL/2\pi}$. Above the threshold the wave drag increases continuously with the velocity. Such continuous imperfect (smoothed) bifurcation was indeed observed in the careful experiments with specially designed ship models by Taylor about a century ago [8]. The critical velocity obtained from the fit of the experimental data agrees rather well with the theoretically predicted value [7].

The dispersion relation for the capillary-gravity waves, on the other hand, exhibits a minimum in the phase velocity V_c at the wave number, which is called the capillary wave number κ. Below V_c the surface waves cannot be emitted, so no wave resistance force acts on the object. Thus, in this case the bifurcation from a no-wave to the wave-generating state is an intrinsic property of the dispersion law and is not related to the size of the perturbing object. The dispersion relation for the surface waves is [1]

$$\omega^2 = gk + \sigma k^3/\rho, \quad (1)$$

where ω is the circular frequency, k is the wave number, ρ is the fluid density, g is the gravity acceleration, and σ is the surface tension. According to Eq. (1), a phase velocity of the waves $c_p = \omega/k$ has a minimum $V_c = (4g\sigma/\rho)^{1/4}$ at the capillary wave number $\kappa = \sqrt{\rho g/\sigma}$ (see Fig. 1). The stationarity condition of the wave pattern in the frame moving with the object leads to [2]

$$\omega = kV\cos\theta, \quad (2)$$

where θ is the angle between **V** and **k**.

Eliminating ω from Eqs. (1) and (2), one finds

$$\cos\theta(k) = c(k)/V. \quad (3)$$

This equation has evidently no solutions for $V < V_c$ and describes the opening of the Cherenkov radiation cone at $V > V_c$ [9]. Generation of surface waves is analogous to the
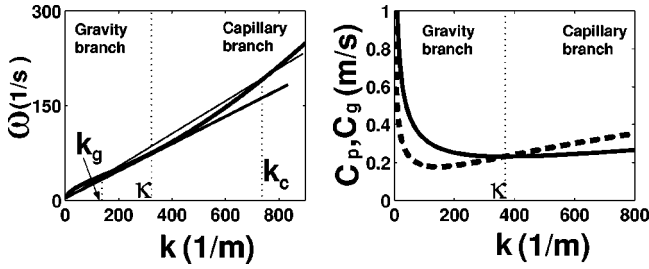
FIG. 1. Dispersion curves for capillary-gravity waves: (a) $\omega(k)$ and (b) wave number dependence of the phase velocity $c_p(k)$ and the group velocity $c_g(k)$.

Cherenkov emission of electromagnetic waves by a charge moving uniformly with a superluminal velocity in a medium. Due to the linear dispersion relation, the Cherenkov radiation of the electromagnetic waves occurs at every wave number into a cone with an opening θ defined by Eq. (3) at c independent of k. Thus, for the linear dispersion, the no-wave region is separated from the wave-generating zone by the Cherenkov cone for electromagnetic waves [9] and by the Mach cone for sound waves [2].

In the case of the nonlinear dispersion law the wave pattern is much more intricate. The pattern of water waves generated by a ship or a body moving over the surface of still water is one of the most common observable phenomena in Nature. The wave pattern follows the moving body unchanged in form, and the waves are confined to a region behind the body that has a V-shaped form in the case of a ship. This wedge-shaped region is called the Kelvin wedge [2]. The dispersive property of the capillary-gravity waves is also responsible for the complicated wave pattern and the shape of the wave-generating region, which will be discussed in this paper later on.

Another difference between waves with linear and nonlinear dispersion laws appears in the range of excited wave numbers. In the case of the capillary-gravity waves, for a given $V \geqslant V_c$, the system of Eqs. (1) and (2) has solutions in the range $0 \leqslant \theta < \chi$, where the angle χ is defined by $\cos \chi = V_c / V$. This range of θ corresponds to the interval $k_g < k < k_c$ of wave numbers resulting from the intersection of Eqs. (1) with a straight line of slope V (see Fig. 1). Therefore, unlike the electromagnetic waves, the capillary-gravity waves are radiated within a finite range of the wave numbers $\Delta k = k_c - k_g$. It tends to zero as $\Delta k = 4\kappa \sqrt{\epsilon}$, when V approaches V_c from above, where $\epsilon = (V - V_c) / V_c$.

The presence of the minimum on the dispersion curve of the capillary-gravity waves [Eq. (1)] results in a gap in the spectrum $\omega(k)$, similar to the gap in the energy spectrum of a superfluid [10]. The existence of the minimum phase velocity for the dispersion curve (1) is analogous to the existence of the Landau critical velocity for the phonon-roton energy spectrum in a superfluid helium [10]. The problem of the drag onset at the Landau critical velocity V_0 due to the radiation of rotons was recently considered theoretically in Ref. [11]. Pomeau and Rica observed the onset of the roton generation at a certain critical velocity in numerical simulations of the generalized nonlinear Shrödinger equation, and pointed out but without proof, that the roton drag force close

to the onset depends on the control parameter $\epsilon = (V - V_0) / V_0$ as $\sqrt{\epsilon}$ in three dimensions (3D) and as $\log \epsilon$ in (2D).

The onset of the wave resistance and its behavior in the supercritical region for the capillary-gravity surface waves was theoretically considered in recent papers [12,13]. Both these papers have studied the wave resistance created by an external pressure distribution that moves with speed V. The difference is that in the first paper both 2D and 3D cases for an inviscid fluid were considered. While in the second paper a 2D case for a low viscous fluid was treated. Both papers used the same Kelvin model. The main result of the calculations for the 3D waves with the point localized pressure distribution (δ-pressure distribution) in Ref. [12] is the prediction of a discontinuous transition to the nonzero wave resistance state at $V = V_c$, if the object size is equal to or smaller than the capillary wavelength $\lambda_c = 2\pi/\kappa$ [12]. It was predicted that the value of the jump in the wave resistance at the transition strongly depends on the surface tension: the jump increases with the decreasing of the surface tension [12].

In order to elaborate further on the theoretical model, we conducted numerical calculations based on the expression (2.33) in Ref. [12] using the following axisymmetric pressure distribution $P(r,b) = b^2 p / 2\pi (1 + b^2 r^2)^{3/2}$, which is one of the presentations of the δ function, p is the total vertical applied force used in Ref. [12], and b^{-1} is the width of the distribution. Indeed, it is easy to be convinced that $\lim_{b \to +\infty} P(r,b) = p\delta(r)/\pi r$, and this pressure distribution is identical to the δ-pressure distribution chosen in Ref. [12]. The Fourier transform of the pressure distribution $P(r,b)$ is $G(k,b) = p g(k,b)$, where $g(k,b) = \exp(-k/b)$. Then the wave resistance can be expressed in the following form:

$$R(x) = \frac{\kappa p^2}{\pi \sigma} x^2 f(x,b), \tag{4}$$

where

$$f(x,b) = \int_0^{\arccos(1/x)} (g(k_c)^2 [\cos \theta^2 - \sqrt{\cos \theta^4 - x^{-4}}]^2$$

$$+ g(k_g)^2 [\cos \theta^2 + \sqrt{\cos \theta^4 - x^{-4}}]^2)$$

$$\times \frac{\cos \theta}{2\sqrt{\cos \theta^4 - x^{-4}}} d\theta. \tag{5}$$

Here $x = V/V_c \geqslant 1$ is used. From the above expressions one can see that at $b \to \infty$ $P(r) = p\delta(r)$, $G(k) = p$, $g(k) = 1$, and

$$f(x) = \int_0^{\arccos(1/x)} \cos \theta \frac{2\cos \theta^4 - x^{-4}}{\sqrt{\cos \theta^4 - x^{-4}}} d\theta,$$

i.e., one comes back to the function presented in Ref. [12] for the δ-pressure distribution. So one can write $\lim_{b \to +\infty} f(x,b) = f(x)$. Our numerical simulations show that with b being fixed at about 10^6 or greater, one cannot distinguish, with the accuracy of the calculations, between the re-
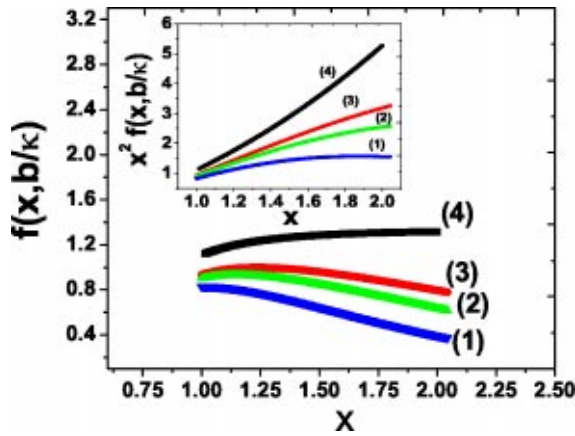
FIG. 2. Dependence of $f(x,b/\kappa)$ on the reduced velocity x for three values of b/κ: (1) 10, (2) 17, (3) 25; curve (4) shows the result from Ref. [12] for comparison. The inset shows the dependence of $x^2 f(x,b/\kappa)$ on the reduced velocity x at the same values of b/κ as on the main plot. Curve (4) shows the result from Ref. [12].

sult of Ref. [12] and the calculation based on our pressure distribution with $f(x,\infty)_{x\rightarrow 1} = \pi/2\sqrt{2}$. Then the jump in the wave resistance at the transition is defined by $\lim_{x\rightarrow 1} R(x) = \kappa p^2/2\sqrt{2}\sigma$ as in Ref. [12]. Thus the difference between the δ-pressure distribution, used in Ref. [12], and the finite-size pressure distribution taken by us shows up just in the functional dependence of $f(x,b)$ on the reduced velocity and the distribution width b^{-1}.

In Figs. 2–4 we present the dependence $f(x,b/\kappa)$ at fixed values of b/κ in the wide range of variation of this parameter. One can find in Fig. 2 that at $b/\kappa \rightarrow \infty$ one recovers the result of Ref. [12] (curve 4 on the main plot and in the inset). At the values of $b/\kappa = 25,17,10$ (Fig. 2) the wave resistance jump at the transition reduces, so that it reduces about 20% at $b/\kappa = 10$ (curve 1 in the inset), and the wave resistance dependence on V/V_c becomes much weaker than in the case of the δ-pressure distribution. Actually at $b/\kappa = 10$ it saturates at $V/V_c > 1.8$. By the way, the value of $b/\kappa = 17$ (curve 2) corresponds to the object size $d = b^{-1} = 0.2$ mm, if one considers the capillary length for water ($\kappa = 2\pi/\lambda_c = 3.696$ cm^{-1}).
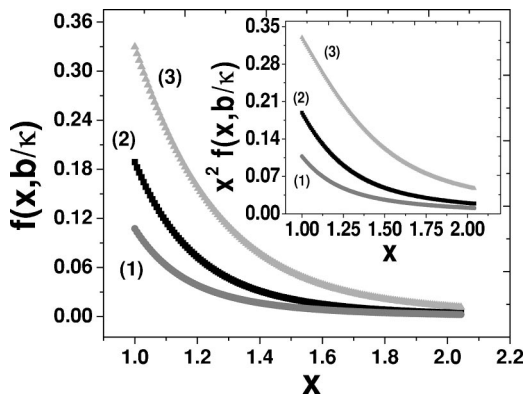

FIG. 3. $f(x,b/\kappa)$ vs x at $b/\kappa = 0.89$ [curve (1)], $b/\kappa = 1.19$ [curve (2)], and $b/\kappa = 1.78$ [curve (3)]. The inset shows the dependence of $x^2 f(x,b/\kappa)$ on the reduced velocity x at the same values of b/κ as on the main plot.
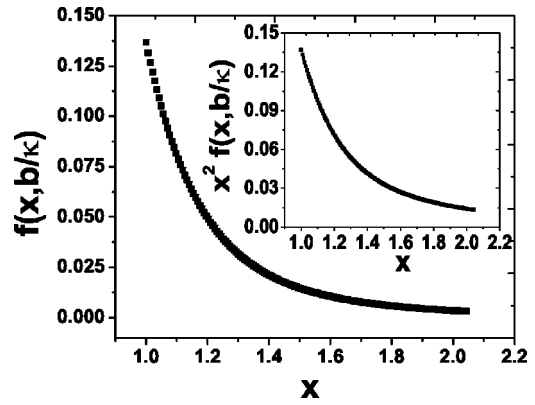

FIG. 4. $f(x,b/\kappa)$ vs x at $b/\kappa = 1$ corresponding to the capillary length. The inset shows the dependence of $x^2 f(x,b/\kappa)$ on the reduced velocity x at the same value of b/κ as on the main plot.

In Fig. 3 we present the calculations for three values of $b/\kappa = 1.78, 1.19, 0.89$ that correspond to three values of the object size $d = 1.57, 2.35, 3.14$ mm, respectively (at $\kappa = 3.696$ cm^{-1}) used in the experiment reported in the paper. In Fig. 4 the dependence $f(x)$ at $b/\kappa = 1$ is presented separately.

From the calculations presented in Figs. 3 and 4 one can conclude that the overall functional behavior of the wave resistance (see the insets in Figs. 3 and 4) contradicts that found experimentally in the experiments reported in the paper. The jump in the wave resistance at the transition remains, though reduced down to about 11% of its value at the transition for the δ-pressure distribution case (see the inset in Fig. 3, the curve 1, which corresponds to the smallest value of b/κ used). Moreover, at small values of b/κ (b/κ below 10 that corresponds to $d > 0.53$ mm at $\kappa = 3.696$ cm^{-1}) the wave resistance is a decreasing function of V/V_c, and this fact also contradicts the common sense. Thus, the finite-size pressure distribution used in the calculations does not change the type of the transition but makes the functional dependence of the wave resistance above transition even more questionable.

Theoretical predictions for a two-dimensional case look even more problematic. The calculations of the wave resistance for an inviscid fluid with the pressure distribution along a line lead to a singular solution at $x \rightarrow 1$ [12]. While more recent calculations [13] showed that including viscosity removes the singularity: the wave resistance increases steeply at the transition but remains bounded. Above the transition $R(x)$ is a decreasing function that once more makes these predictions doubtful.

A very recent paper by Sun and Keller [14] deals with the wave resistance dependence on the velocity of a moving object far away from the bifurcation. It is basically an extension of the theory presented in Ref. [12] to the region of the velocities far away from the bifurcation. So, a comparison of the predictions of this paper is beyond the scope of our paper.

Recently the results of two experiments on the onset of the capillary-gravity wave resistance were reported [15,16]. The conclusions of these two experiments contradict each other. While the authors of Ref. [15] claim that the experi-

ment shows a discontinuous transition to the wave drag state in agreement with the theory [12], the conclusion of Ref. [16], which is a short version of the current paper, is that the transition is continuous (smooth). This discrepancy and a comparison with the results of the experiment by others [15] will be discussed in this paper.

In this paper we investigate the dependence of both the wave drag force and the capillary-gravity wave pattern on the object velocity V in the vicinity of the transition for various fluids and object sizes on the air-fluid and fluid-fluid interfaces. The results of the experiments clearly demonstrate that the transition to the wave drag state is a continuous one, in contradiction to the theoretical prediction [12], as well as the behavior of the wave resistance as a function of the object velocity above the threshold is drastically different from the predicted one [12,13].

The paper is organized as follows. The details of the experimental setup of calibration and experimental procedure are given in Sec. II. Section III presents the experimental results on the wave drag for both air-fluid and fluid-fluid interfaces. Then the experimental results on the wave drag are discussed and compared with the theory and with the experiment by others in Sec. IV. The experimental observations and the results of theoretical calculations of the wave pattern and the shape of the wave wedge are given in Sec. V. Finally, the conclusions are presented in Sec. VI.

II. EXPERIMENTAL SETUP AND EXPERIMENTAL PROCEDURE

A. Experimental setup

Experiments were conducted in a circular rotating channel of 12.4 cm outer radius and 3.6 cm gap, made of plexiglass, with a stainless steel ball, as an object, suspended on a thin tungsten wire, which is glued to a thin elastic made of acrylic polymer fiber. For visualization, we used also a larger gap channel with outer radius 17.5 cm and 15 cm gap. The gap size of the channel was chosen to ensure visualization of a wave pattern from above as well as from below. A smaller gap could lead to wave reflection from the channel walls that could complicate pattern interpretation. The channel was driven by a stepping motor via a belt transmission with ratio 0.138 and with a velocity controlled better than 0.02%. A dc brushless motor with an optical encoder for feedback velocity control as another option was also used to compare its performance with the stepping motor. The main concern was insufficient smoothness of the stepping motor drive and its influence on the experimental data, particularly in the vicinity of the critical velocity. The comparison showed that the stepping motor drive does not affect the data. Balls of various diameters d (1.57, 2.35, and 3.14 mm) and a tungsten wire and a fiber made of acrylic polymer (0.3 and 0.7 mm diameter, respectively) half-immersed into a fluid, were used. Each of them is smaller than λ_c for any fluid used in the experiments.

The main idea of the setup is to measure the force on the ball without allowing it to move from the initial (zero velocity) position by using an appropriate feedback loop. The reason for this is the following: if the ball moves, the contact
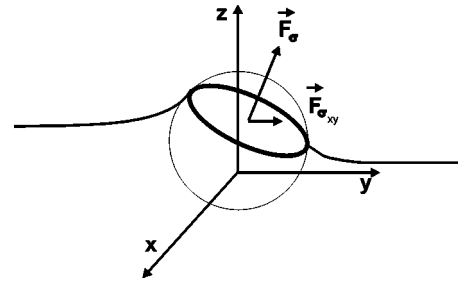

FIG. 5. The capillary contribution to the measured force in the case of wetting. The ball is allowed to move.

curve between the fluid and the ball's surface tilts with an angle approximately equal to the deviation angle of the wire (Fig. 5). Thus, the capillary force (which, in this case, is normal to the contact line's plane, and its magnitude is proportional to the length of the contact line) will make a nonzero angle with the vertical direction providing an additional force component on the direction of the flow (y direction). The magnitude of this component is not negligible. For example, in the case of water and a 3.14-mm-diameter ball, the capillary force is almost 200 times larger than the viscous drag. So the tilted contact line can smear out almost completely the transition to the wave drag state [16]. This nonnegligible contribution to the measured force is not the only reason for holding the ball in the same initial vertical position during the force measurements. The second reason is that the capillary force is hysteretic and leads to random discontinuous variations in the force measurements. We have observed this effect in the experiments conducted with a metallic wire and a fiber immersed into a fluid (see below). Thus, hysteretic behavior of the capillary force would interfere with the drag force variations due to the transition itself and would complicate a decision on the nature of the transition to the wave-generating state. As we will show below it is the case in the experiment described in Ref. [15].

Our way to hold the ball in the initial position was to exert a magnetic force applied to the ball via the proportional-integral feedback loop. The latter was activated via eddy current commercial displacement gauge (EMD 1050 Electro Corporation), used as a position sensitive detector to measure a deviation of a brass cylinder (2 mm diameter), mounted on the same wire as the object itself, from its initial position. A signal from the displacement detector drives via instrumentational amplifier and power amplifier (PS) two electromagnetic coils, which provide the magnetic force to hold the ball in the initial position [see Fig. 6(b)]. A current supplied to the coils is calibrated as a force. The coils are designed in such a way that the magnetic force experienced by the metallic ball is proportional and always opposite to the deviation of the wire from the initial vertical position. One should mention that in our setup it was impossible to activate the feedback with a ball of less than 1.5 mm diameter. Indeed, the viscous drag reduce with a radius between linear and square dependence but the stabilizing magnetic forces reduces in a third power [see further Eq. (8)]. It means that for the parameters of the coils used for the feedback, and the object velocities observed in the experiment, one is limited by the ball diam-
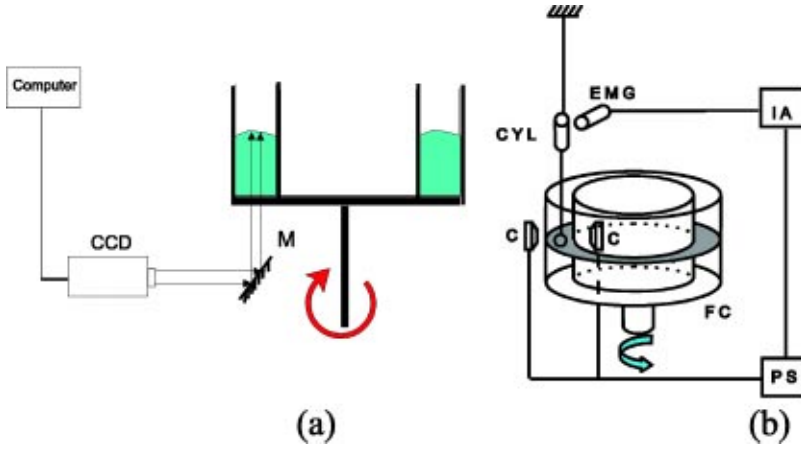
FIG. 6. Experimental setup: (a) wave visualization; (b) force measurements. FC, channel with a fluid; CYL, cylinder to measure a deviation from an initial position by eddy current gauge (EMG); IA, amplifier; and PS, power apmlifier; C; electromagnetic coils.

eter in order to fix it in the initial position by the magnetic force.

Light refraction visualization [see Fig. 6(a)] was also used to define the onset of the surface waves generation, the wave pattern, the shape of the wave-generating region, and the wave numbers as a function of velocity. As working fluids water, silicone oils DC200 of the kinematic viscosity $\nu = \eta/\rho = 10$ and 50 cS and of the surface tension $\sigma = 20.1$ and 21.2 mN/m, respectively, water-glycerin mixtures of $\nu = 10$, 30, and 46 cS and almost the same $\sigma = 66$ mN/m, were used (see Table I). The depth of each fluid was sufficiently large to ensure the validity of an infinite depth approximation for the surface waves.

B. Calculation of the magnetic field and magnetic force exerted on a body

A body placed in a magnetic field **H** experiences a magnetic force:

$$\mathbf{F_m} = \chi \int \int_v \int \nabla \mathbf{H^2} d\tau, \tag{6}$$

where χ is the magnetic susceptibility of the body and v stands for its volume. In the case the object is small enough with respect to the characteristic length of the magnetic field variation $(\mathbf{H^2}/\nabla \mathbf{H^2})^{1/2}$ (that means that the field changes slowly over the volume of the body), Eq. (6) may be written as

$$\mathbf{F_m} \approx \chi v \nabla (\mathbf{H^2}), \tag{7}$$

where $v = \pi d^3/6$ is the volume of the object. A simple estimate of the magnitude of the minimum necessary magnetic field to hold an object below the transition to the wave drag state can be obtained by equating the magnetic force and the Stokes drag:

$$\nabla \mathbf{H^2} = \frac{18\eta V}{\chi d^2}, \tag{8}$$

where η is the kinematic viscosity of the fluid.

It is clear that above the threshold the magnetic force should exceed the value given by Eq. (8) in order to hold the ball in the initial position. From Eq. (8) one can conclude that a proper design of the magnetic coils should, first of all, ensure a sufficiently large value of $\mathbf{H}\nabla\mathbf{H}$, and not only of the field itself. In order to correctly design the coils and to find the ball location in relation to the magnetic field geometry to maximize its interaction with the field, numerical simulations of a system of coils, arranged symmetrically with respect to the flow direction and fed by opposite currents were performed (see, e.g., Ref. [17]).

As the result of the calculations it was found for $I = 4$ A and $N = 300$ that the maximum of the magnetic force is reached if the ball is placed in the vicinity of the middle point in the space between coils and slightly off the central line. These theoretical estimates have been experimentally

TABLE I. Physical properties of fluids used in the experiments (at 25 °C), values of V_c (theoretical and experimental), λ_c, and κ.

		Glycerin-water 60.4%	Glycerin-water 74.5%	Glycerin-water 79%	Silicone oil DC 200/10	Silicone oil DC 200/50
	Water					
η (cP)	1	11.06	35.7	55.3	9.34	48.5
ν (cS)	1	9.6	30	46	10	50
σ (mN/m)	73	66	66	66	20.1	21.2
ρ (kg/m^3)	998	1152.2	1190.5	1202.7	934	970
V_c Theor.	0.231	0.218	0.216	0.215	0.17	0.171
(m/s) Expt.	0.213	0.195	0.2	0.195	0.165	0.183
λ_c(m)	0.017	0.015	0.0149	0.0149	0.0093	0.0094
κ (m^{-1})	369.6	413.8	420.6	422.8	675.2	670

FIG. 7. Magnetic coil design.

FIG. 8. The forces acting on the pendulum: F_m is the magnetic force; F_{el} is the restoring force of the thin fiber F.
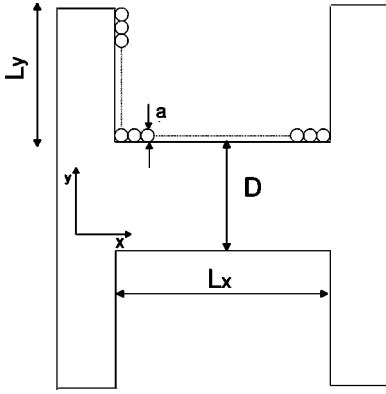
verified by measuring the field at different locations in the space between coils with a Hall effect magnetometer (Oxford 5200).

C. The design of the magnetic coils

Space limitation particularly for the inner coil imposes the main restrictions on the coil design. It first of all concerns a cooling system: air cooling can be only used instead of a water-cooling system. The design of the coils is shown in Fig. 7. The optimization of the design (selection of the wire diameter a and one of the characteristic sizes of the coil, L_y, at the fixed value of another size, $L_x = 24$ mm) is a compromise between the maximum possible magnitude of the magnetic field and the minimum possible heat dissipation. As a result the optimal value of the dissipated power at the selected wire $a = 1.3$ mm and the number of turns $N = 300$ is about 90 W. Since each run lasts for a rather long time to average the current data, significant heating of the coils requires at least air cooling. In spite of this the coil temperature is raising with time, and one should correct the measured values of the current for the temperature variation of the coil resistance. So, for this reason, a thermistor in a coil was installed, and the coil temperature was recorded along with the current. Then on each time step j of the sampling, the measured value of the current was corrected according to

$$I_{j,c} = \frac{I_j}{1 - \alpha(T_j - T_{init})R_{init}/R_j}, \tag{9}$$

where $I_{j,c}$ is the corrected value of the current at the time step j, I_j is the measured value of the current at the time step j, α is the thermal coefficient of the coil resistance, T_j and T_{init} are the coil temperatures at the time step j and at the initial moment (at the ambient temperature), R_j and R_{init} are the coil resistances at the time step j and at the beginning of the experiment. From Eq. (9) it is rather clear that the effect of the coil heating leads to a suppression of the measured current and even its saturation at a certain velocity of the object if the temperature variation is rather substantial. It means that during the experiment, when the coil temperature changes with time, the measured value of the current on each step depends not only on the object velocity, but also on the coil temperature at each step, i.e., $I_j = I(V_j, T_j)$. Thus, the
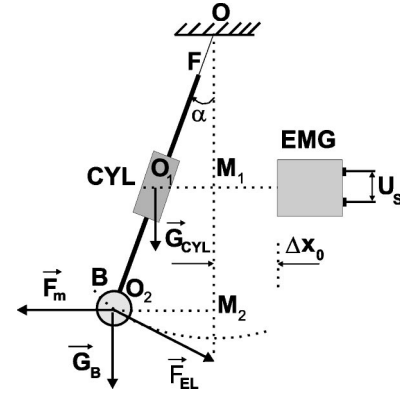
thermal corrections are of crucial importance to obtain real values of the force exerted on the object.

D. Force calibration and parameter selection of the feedback loop

Since the magnetic field generated by a coil is proportional to the current applied, the magnetic force is proportional to the square of the current if the field changes on the characteristic length much larger than the ball size. The goal of the calibration procedure is to find the coefficient K_m in relation between the force and the current, $F_m = K_m I^2$. As the first step, the position sensitive sensor was calibrated. This was done by moving a metallic object mounted on a micrometer. Measuring the voltage output of the sensor, U_s, versus the distance of the object from the sensor, Δx, provides the calibration curve. The result of the linear fit of the calibration curve gives $U_s = n\Delta x + m$, where $n = 0.011\,12 \pm 0.000\,04$ V/μm and $m = 2.303 \pm 0.0050$ V.

As the next step, the magnetic force calibration was conducted by suspending in still air, between two coils a pendulum shown in Fig. 8. Then, for each value of the current feeding the coils, the signal of the sensor, calibrated in units of distance, was recorded. The deviation $\Delta x = O_1 M_1$ (Fig. 8) of the pendulum can be related to the forces applied to it, by writing the torque balance condition (the restoring elastic force of the thin fiber was neglected as being extremely small). As a result the sensor signal can be related to the measured parameters of the system and the coefficient K_m by the following expression:

$$U_s = n\Delta x_0 + m + \frac{cL_2 K_m I^2}{\sqrt{g^2(m_b L_2/L_1 + m_{cyl})^2 + K_m^2 I^4 (L_2/L_1)^2}}, \tag{10}$$

where $g = 9.81$ m/sec^2, $m_b = 0.14$ g, $m_{cyl} = 0.2$ g, $L_1 = 3.5$ cm, $L_2 = 2.5$ cm. The calibration data together with the nonlinear fit by Eq. (10), is shown in Fig. 9. The corresponding parameters of the fit were found to be $\Delta x_0 = 200 \pm 0.05$ μm and $K_m = 2.993 \times 10^{-7} \pm 5 \times 10^{-10}$ N/A^2.

Another issue that deserves attention is the characteristic time of the proportional-integral feedback loop. During regulation of the object location via the feedback loop the ball
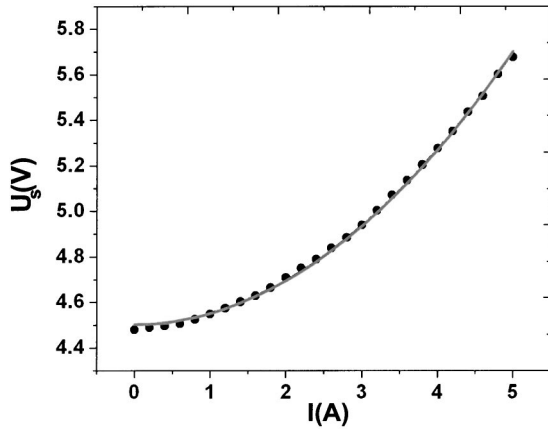
FIG. 9. Calibration data for a 3.14 mm ball in air (full circles) and the nonlinear fit (full line).

FIG. 11. The reduced wave drag force vs the reduced velocity for three fluids and a 3.14-mm-diameter ball: squares, silicone oil DC200/50 cS; circles, glycerin-water 30 cS; triangles, glycerin-water 46 cS. The inset: the same for water. Solid curves on all plots are the fits by the Landau equation with a field (see text).

oscillates around an equilibrium position. A correct force measurement by this technique assumes that the feedback oscillations do not interfere with the flow. It means that the characteristic time and the amplitude of the current fluctuations should be much smaller than the characteristic time of the flow and the average current values, respectively. In the case of the resonant feedback regulation, the current oscillation amplitude can reach as large as about 6% of the average current value. So the resonance regime should be avoided. In an overdamped regime of the feedback loop, which was obtained by tuning the integration time and the gain, the current fluctuations are remained as small as 0.5%.

III. EXPERIMENTAL RESULTS

A. Wave drag force as a function of the object velocity for various air-fluid interfaces

The raw data on the full drag force F as a function of the channel velocity for silicone oil (10 cS)-air interface and a ball with $d=3.14$ mm are presented in Fig. 10. The data taken with increasing and decreasing values of velocities are reproducible and show no hysteresis. Analogous data for $d=2.35$ and $d=1.57$ mm balls were also obtained and are
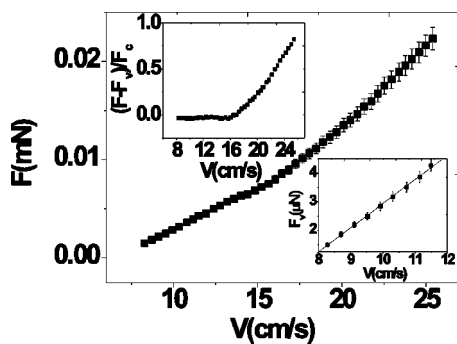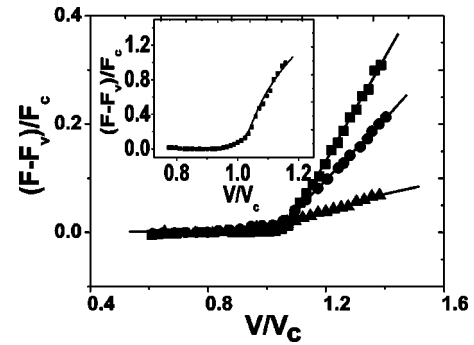

FIG. 10. The drag force vs the velocity for silicone oil DC200/10 cS and a 3.14-mm-diameter ball. The upper inset: the same data but for the reduced force. The lower inset: the viscous drag force below the transition vs the object velocity. Solid line is the second-order polynomial fit.

shown below. Since the critical velocity of the transition to the wave-generation state is rather low, the critical Reynolds numbers at the transition for different fluids and ball sizes are in the range between 2.2 (for a 1.57-mm-diameter ball and silicone oil 50 cS) and about 700 (for the 3.14-mm-diameter ball and water). It means that below the transition the drag consists of a viscous Stokes drag at Re$\leqslant 1$, which changes linearly with V, and the drag, proportional to V^2, due to the eddy viscosity for the Reynolds numbers up to Re$\sim 10^3$ [1]. The data below the transition fitted by a second-order polynomial give a reasonable value of the Stokes drag (see the lower inset in Fig. 10, where the fit gives $\nu=8.4$ cS instead of 10 cS). Then by subtracting the viscous drag one obtains the reduced wave drag force $(F-F_v)/F_c$ as a function of the object velocity. This plot clearly exhibits the continuous bifurcation to the wave drag state at $V_c=16.5$ cm/sec, which is rather close to the theoretical value of 17.0 cm/sec (see Table I). Here F_v, F_c are the viscous drag force and the critical value of the drag force at the onset, respectively.

The rest of the data is shown in the reduced variables, which are convenient to compare the data for different ball sizes and different fluids. Figure 11 shows the data of the reduced drag force versus the reduced velocity for four different fluids with the 3.14-mm-diameter ball: silicone oil (50 cS), glycerin-water (30 cS), glycerin-water (46 cS), and water. It is obvious from the plots that the increase in the wave drag force strongly depends on fluid properties (ν and σ). We would also like to point out that the wave drag for water (see the inset in Fig. 11) increases very dramatically (the vertical scale is larger).

Another set of data for water and silicone oil (50 cS) with a 2.35-mm-diameter ball is presented in a scaled form in Fig. 12. We found experimentally that the data for each ball size and different fluids can be collapsed on a single curve if the reduced drag force $[(F-F_v)/F_c]_i$ is multiplied by a factor $\nu_i\sigma_i$, where $i=1,2,3,\ldots$. Moreover, the data for the reduced drag force for different fluids and different ball sizes can be collapsed on a single curve with rather good accuracy being multiplied by the factor $\nu\sigma/d^2$. In Fig. 12 two sets of data for silicone oil (50 cS) are shown. The data are rather similar, except a dimple on one curve before the onset of the
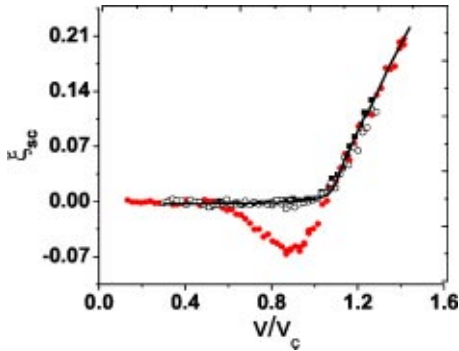
FIG. 12. The reduced scaled wave drag force ξ_{sc} vs the reduced velocity for two fluids and a 2.35-mm ball: squares, water; circles and open hexagons, silicone oil DC200/50 cS (see text for definition).

FIG. 14. The reduced wave drag force vs the velocity for a silicone oil DC200/50 cS and a 3.14-mm-diameter ball: full squares, with feedback, open squares, without feedback.

wave generation. Such a dimple was sometimes observed for all sizes of balls but more pronounced for smaller sizes in a case, when silicone oil was used as a fluid. Silicone oil does not wet the ball surface, and as a result a convex meniscus is formed. The observed dimple results from a meniscus position instability, which depends on the initial location of the meniscus, on properties of the ball surface, and pressure redistribution over the ball surface with increasing fluid velocity. The dimple depth strongly depends on the initial location of the meniscus and cleanliness of the ball surface, which both were not well controlled. The latter results in rather random values of the dimple depth observed. The observed decrease in the value of the reduced drag force is caused by the interface instability, which leads to a relocation of the meniscus position down and the corresponding reduction in the drag force.

Finally the last set of the data for the ball size of 1.57 mm diameter and four different fluids (glycerin-water with three values of viscosity 10, 30, and 46 cS, and silicone oil of 50 cS) is presented also in the scaled form in Fig. 13. As one can mention the data for glycerin-water 10 cS exhibit a weak bump and the data for silicone oil show a slight dimple just before the transition. Glycerin-water solution wets and silicone oil does not wet the ball. So the possible interface instability in these two cases leads to relocation of the menis-

cus in opposite directions and to correspondingly opposite contributions into the drag force.

Thus, all the data demonstrate that the transition to the wave drag state is continuous, and the quality of the bifurcation is about the same for all ball sizes and all fluids. It is rather surprising that such strong perturbation as an additional interface instability before the bifurcation into wave-generating state does not change the type of the bifurcation.

To emphasize the role of the contact line relocation due to the ball displacement, two sets of data, one with the feedback on as in Fig. 10, and another with the feedback off are shown in Fig. 14. Since the capillary force exceeds the wave drag force near the onset, the relocation of the contact line due to the ball displacement and the variation in the capillary force in this way diminish partially or completely the contribution of the wave drag into the force measurements. So, the transition is almost smeared out in the measurements without the feedback.

B. Wave drag force as a function of the object velocity for various fluid-fluid interfaces

We also conducted experiments on the wave drag with a ball located on the interface between two fluids. The idea was to reach a small critical velocity due to a reduction of the surface tension on the fluid-fluid interface and due to a small difference in fluids densities. Indeed, the corresponding expressions for the critical velocity

$$V_c = [g\sigma(\rho_1 - \rho_2)]^{1/4}\sqrt{2/(\rho_1 + \rho_2)} \tag{11}$$

and the capillary wave length

$$\lambda_c = 2\pi\sqrt{\sigma/g(\rho_1 - \rho_2)} \tag{12}$$

are modified in this case compared with an air-fluid interface [3].

As the experiments show, the critical velocity e.g., for the water-silicone oil (10 cS) interface, was indeed found as low as $V_c \approx 4$ cm/sec (see Fig. 15). It corresponds to rather low surface tension of $\sigma = 3.7$ dyn/cm. The data clearly exhibit a pretransitional bump, which is related to the interface instability discussed above. For a fluid-fluid interface with one wetting and another nonwetting fluid, the meniscus position is more susceptible to the instability than an air-fluid inter-
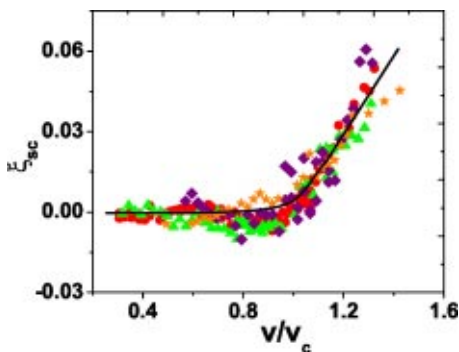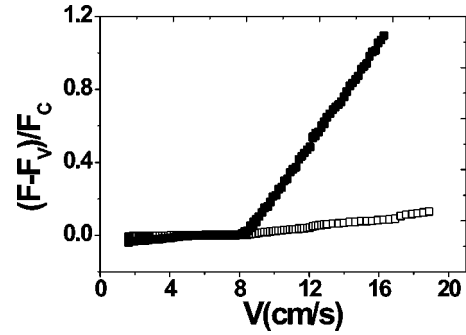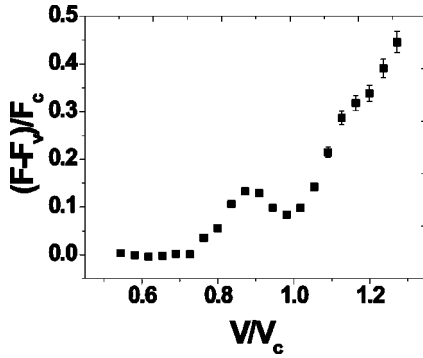

FIG. 13. The reduced scaled wave drag force ξ_{sc} vs the reduced velocity for four fluids and a 1.57-mm-diameter ball: circles, silicone oil DC200/50 cS; stars, glycerin-water 10 cS; triangles, glycerin-water 30 cS; diamonds, glycerin-water 46 cS.

FIG. 15. The reduced drag force vs the reduced velocity for water-silicone oil DC200/10 cS interface and a 3.14-mm-diameter ball.

FIG. 17. The drag force vs the velocity for glycerin-water (10 cS)-silicone oil DC200/10 cS interface and a 2.35-mm-diameter ball.

face. It results in a stronger effect on the drag force and even sometimes in the exchange of a bump to a dimple with velocity increase, which was observed in the experiment.

Another two sets of the data for a pair of water and silicone oil (50 cS) interface with the 3.14-mm-diameter ball (Fig. 16), and glycerin-water (10 cS) and silicone oil (50 cS) interface with 2.35 mm diameter ball (Fig. 17) show a regular continuous transition to the wave resistance state, similar to that observed for an air-fluid interface. For the latter pair of fluids, the surface tension was measured separately by weighing an injected drop of a heavier fluid (glycerine-water) into another fluid (silicone oil) at the moment of detachment from a capillary. The measured value of the surface tension in this case was $\sigma = 17.7$ dyn/cm that gave $V_c = 7.65$ cm/sec. This value of V_c was found to be in a good agreement with the experimentally found value of $V_c = 7.8$ cm/sec from the wave drag force measurements (see Table I). Thus, the data for the fluid-fluid interface for several fluid pairs and two ball sizes also exhibit the continuous transition from no-wave to the wave-generating state.

IV. DISCUSSION OF THE WAVE DRAG DATA AND THE COMPARISON WITH THE THEORY AND OTHER EXPERIMENTS

A. Analysis of the experimental data

Let us discuss the experimentally found scaling, which allows us to collapse all the data for the reduced wave drag
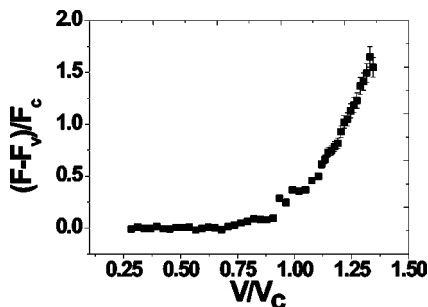

FIG. 16. The reduced drag force vs the reduced velocity for water-silicone oil DC200/50 cS interface and a 3.14-mm-diameter ball.
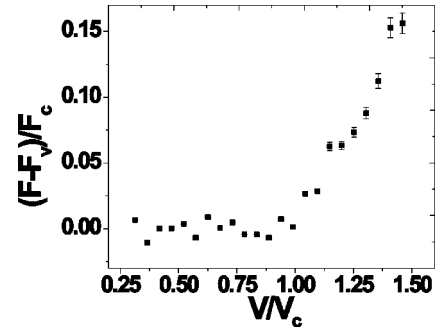
force versus the reduced velocity on a single curve. First, we checked the scaling of $F_c \equiv F(V_c)$, which we use to provide a dimensionless variable to the wave drag force. As a result, for all fluids and all ball sizes used in the experiment, one finds $F_c = F_0 \eta V_c d$ with the dimensionless parameter $F_0 = (0.47 \pm 0.02) \times 10^{-6}$. Second, using this scaling relation and another scaling relation mentioned before, one can write $(F - F_v)/F_0 \sim (\rho d^3 V_c / \sigma) f(V/V_c)$. It means that the wave drag is viscosity independent in the range of parameters used in the experiment. Thus, it indicates that the observed drag force is indeed caused by the wave emission only, and there is no measurable contribution of the increase in the viscous drag force due to possible contact line relocation.

The next problem is the dimensionality of the scaling found empirically. The scaling found experimentally at first sight contradicts the dimensional analysis. Indeed if one assumes that the only relevant physical parameters of the problem are $(\sigma, \rho, g, \nu, d)$, then, according to the Buckingham π theorem [1], one can express the reduced wave drag force in the following functional form:

$$\frac{F - F_v}{F_c} = f\left(\frac{V}{V_c}, \mathrm{Re}_c, \kappa d\right),$$

where $\mathrm{Re}_c = d V_c / \nu$ is the Reynolds number at the threshold velocity, and V_c and κ are as defined earlier. The functional dependence on d is experimentally established rather firmly. So the only possible scaling in this case may be $(F - F_v)/F_c = (\mathrm{Re}_c \kappa d) f(V/V_c)$ that leads to the dependence on σ incompatible with the experimentally found. Thus the only possible simple resolution of this scaling problem is a suggestion that there exists another relevant parameter—the channel width h. Indeed, as we pointed out, the data on the drag force were taken in a rather narrow channel of $h = 3.6$ cm, where wave reflection was significant. Introducing an additional parameter in the problem allows one to add another nondimensional parameter, namely, κh. So the reduced wave drag force can be rewritten in this case as

$$(F - F_v)/F_c = (\mathrm{Re}_c \kappa d (\kappa h)^\beta) f(V/V_c), \qquad (13)$$

where the exponent β can be defined from the requirement to satisfy the experimentally found scaling in σ. Then one gets $\beta = 3/2$. Thus the final functional dependence is
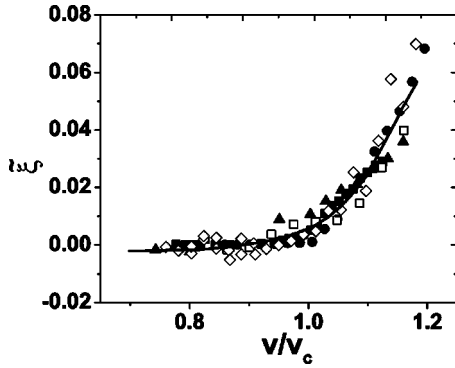
FIG. 18. The reduced wave drag force divided by the nondimensional parameter A, $\tilde{\xi}$, vs the reduced velocity for five different fluids with a 3.14-mm-diameter ball, except otherwise mentioned: full squares, water; full circles, silicone oil DC200/50 cS; triangles, glycerin-water 46 cS; open squares, glycerin-water 30 cS; open diamonds, silicone oil DC200/50 cS, a 2.35-mm ball (see text for definitions).

$$\frac{F-F_v}{F_c} = Af\left(\frac{V}{V_c}\right), \tag{14}$$

where the nondimensional parameter is

$$A = \mathrm{Re}_c\, \kappa d(\kappa h)^{3/2} = \sqrt{2}\, \frac{d^2}{\nu\sigma}(gh)^{3/2}\rho, \tag{15}$$

i.e., we can recover the experimentally found scaling factor $d^2/\nu\sigma$ compatible with the dimensional considerations [18].

Since we observed experimentally the continuous transition to the wave drag state, it is natural and widely employed to use the stationary Landau equation as a fit to the data to extract the values of the critical parameter (V_c in this case), the nonlinear coefficient a, and the "field" h_1, which plays a role of the smearing factor. The inset in Fig. 11 presents the data for water with the 3.14-mm-diameter ball in the narrow range of the control parameter together with a fit by the stationary Landau equation with a field: $\epsilon\xi - a\xi^3 + h_1 = 0$, where $\xi \equiv (F-F_v)/F_c$ is the order parameter, $\epsilon \equiv V/V_c - 1$ is the control parameter. A similar fit was used for all sets of the data presented in the scaled variables $\xi_{sc} = \xi\nu_i\sigma_i d_i^{-2}/\nu_1\sigma_1 d_1^{-2}$, where the subscript "1" defines a fluid, relatively to which the rest of fluids with the subscripts $i = 1,2,3,\ldots,$ are scaled (see, e.g., the fits in Fig. 11 for three separate sets of the data, in Fig. 12 for two sets of the data, and in Fig. 13 for four sets of the data). In Fig. 18 we present the data for various fluids and ball sizes in the vicinity of the transition by using the wave drag force divided (scaled) by the dimensionless parameter A derived above [Eq. (15)]. All the data collapse onto a single curve although the scaling is not perfect (see Fig. 18 for five different sets of the data). In the same plot we show also the fit by the stationary Landau equation $\epsilon\tilde{\xi} - \tilde{a}\tilde{\xi}^3 + \tilde{h} = 0$, where $\tilde{\xi} = \xi A^{-1}$, and $\tilde{a} = 31.24$ and $\tilde{h} = 0.001\,52$ are constants of the fit independent of the physical parameters of the problem.

Thus, the transition to the wave drag state is continuous, and the drag force behaves above the threshold as $(F-F_v) \sim \sqrt{V-V_c}$.

B. Comparison with the theory

Thus, the experiments presented show unambiguously that the transition to the wave resistance state is continuous one, contrary to the theoretical prediction for the capillary-gravity waves [12]. What can be the reason for this discrepancy? Since solving a full hydrodynamical problem of a flow past a body on either an air-fluid or fluid-fluid interface is a formidable task, the theory considers a model of a moving-pressure distribution [12]. The main difficulty in this theoretical approach is to choose a correct model description. The theory is based on the Kelvin model [4], which is a reasonable approach to long wavelength gravity waves [7]. Instead of a real shiplike object, Kelvin considered a moving-pressure point applied along its course on a water surface [4]. In the case of an object much larger than λ_c, one can neglect a pressure redistribution due to capillary effects, and the Kelvin model works extremely well for the long gravity waves. In the opposite case, when the object size is smaller than λ_c, the capillary force is much larger than all other forces, namely, gravitational and wave drag forces. Then the relocation of a contact line causes redistribution of the pressure. That results in a bump behind the moving object observed in experiments. This factor makes the applicability of the Kelvin model questionable.

C. Comparison with experiments by others

Recently another group has published the results of rather similar experiments on the onset of the capillary-gravity wave resistance [15]. As pointed out in the Introduction, the authors of Ref. [15] came to the conclusion that the transition to the wave drag state is a discontinuous one, in agreement with the theory [12]. Let us discuss deficiencies and shortcomings of this experiment.

There are two main differences between the experiment presented in Ref. [15] and our experiment. First, as a disturbing object, a very thin wire ($d = 0.2$ mm) submerged by a few tenths of millimeters into a fluid was used in the experiments of Ref. [15]. And second, the deflection of the wire from the vertical position, which is proportional to the exerted force by fluid, was measured optically [15]. As was explained in the paper [15], the reason to use so thin wire as a moving body was to satisfy the condition of smallness of the object size compared with the capillary wavelength [15]. In the authors opinion, only in this case the capillary-gravity waves should be generated [15]. Indeed, in this experiment the condition $d/\lambda_c \ll 1$ was satisfied.

We would like to point out that this condition was not required by the theory, because the theory does not use either d/λ_c or κd as a small parameter to get the final result on the wave resistance. Since the theory deals with the onset of the wave resistance near the minimum of the dispersion curve at the minimal critical velocity, it considers capillary-gravity waves, which only appear near this minimum with the wavelength around λ_c. So, the only condition that the experiment
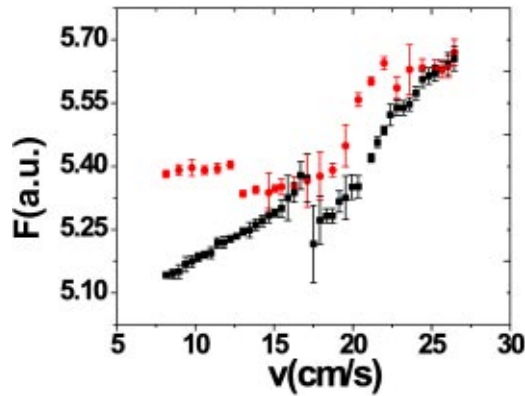
FIG. 19. Drag force as a function of velocity for a wire of 0.3 mm diameter in water: squares, the data taken at increasing velocity; circles, on the way back.

should satisfy is to excite just these waves but not of a larger wavelength, that an object of a size $d < \lambda_c$ can probably generate. Thus, the condition $d/\lambda_c \ll 1$ is not necessary in order to ensure the generation of the surface waves with the wavelength of about λ_c. As was shown, e.g., in our experiment, the capillary-gravity waves can be produced by an object of a size just comparable with λ_c. The most important evidence of the correctness of this statement is the measured value of the critical velocity and the wavelength of the surface waves, generated at the onset. We further discuss this issue studied in our experiment by using a visualization technique.

Another possible reason (not mentioned in Ref. [15]) to use a very thin wire as a disturbing object in Ref. [15] is the δ-pressure distribution used in Ref. [12] to get the analytical functional dependence of the wave drag on the object velocity. However, as our calculations based on the theory of Ref. [15] show, the finite size pressure distribution does not change the nature of the transition, which remains a discontinuous one. Thus this reason does not justify the use of a very thin wire as a disturbing object.

On the other hand, using a thin wire and its deflection as a measure of the force creates an experimental problem due to the increasing contribution of the capillarity and wetting. The data presented in Fig. 1 of Ref. [15] are very scarce and of poor quality to make a particular conclusion about the transition. It is particularly apparent in the vicinity of the transition, which the authors interpreted as a discontinuous one. As one can be easily convinced by the plot, the error bars at the transition are of the same order as the force variations. Unfortunately, the authors did not mention what is the reproducibility of the data if the measurements are taken with the velocity increase and then on the way back. Does the hysteresis exist?

Thus, the statement made by the authors of Ref. [15] that the experimental results are in a good agreement with the theory, is based, first, on their interpretation of the strong scatter of the data at the transition as the discontinuous one, and second, on the assumption that the pressure, used in the theory, is defined through the capillary force. It is just a suggestion that is not tested by the experiment, and other assumptions can be considered as equally probable. So, we suggest that the quantitative agreement claimed in Ref. [15]

is a pure accident. Moreover, much more robust prediction of the theory for δ or very small width pressure distribution that the wave drag above the transition should increase as V^2 contradicts strongly their data. The data of Ref. [15] show decrease of the wave drag force above the threshold. Thus, as we can judge, there is no agreement between their data and the theory even in functional dependence.

We already clearly demonstrated experimentally the role of the capillarity and wetting by switching off the feedback control, as we discussed above. Moreover, in order to further clarify this issue and to drastically increase the role of the capillary force in a force balance with the viscous and wave drag forces, we used a thin wire as an object. We present in Figs. 19–21 the data on the wave resistance in the vicinity of the transition for a fiber of 0.7 mm diameter in water and silicone oil (10 cS) and for a wire of 0.3 mm diameter in water with an immersion depth of the order of its diameter. No feedback was applied. Different symbols mark the measurements due to velocity increase and decrease. Huge hysteresis and scatter particularly for silicone oil in the vicinity of the transition are clearly observed.

As we already pointed out above, when the feedback is off, the position of the meniscus is changed during the experiment due to wire (or fiber) bending under the viscous and wave drag forces, and particularly in the vicinity of the transition to the wave drag state. So the fiber (or wire) bending redistributes and alters the capillary force, which is orders of magnitude larger than the force due to the wave drag to be measured. Moreover, wetting and the capillary force are
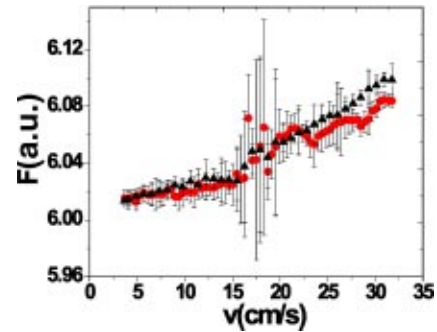

FIG. 20. Drag force as a function of velocity for a fiber of 0.7 mm diameter in water: circles, the data taken at increasing velocity; triangles, on the way back.
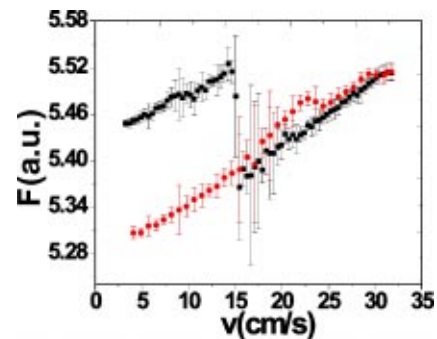

FIG. 21. Drag force as a function of velocity for a fiber of 0.7 mm diameter in silicone oil DC200/10 cS: circles, the data taken at increasing velocity; squares, on the way back.

FIG. 22. Image of the capillary-gravity surface waves generated on water by a 3.14-mm-diameter ball.

FIG. 23. Cos θ of the Cherenkov cone as a function of the velocity for the capillary-gravity surface waves on water. The solid line is calculation based on Eqs. (1) and (3) using the data on $k(V)$, presented in the inset.

strongly hysteretic, particularly on surfaces, to which a specific cleaning treatment procedure was not applied. The pinning and stick-slip motion of the meniscus on a contaminated surface can cause strong force fluctuations and large scatter. Exactly this effect leads the authors of Ref. [15] to an erroneous conclusion about the type of the transition to the wave drag state.

V. WAVE PATTERN AND WAVE NUMBER SELECTION AS A FUNCTION OF THE OBJECT VELOCITY: EXPERIMENT AND CALCULATIONS

The dispersive property of the capillary-gravity waves is responsible for the intricate wave pattern produced by a moving object on an air-fluid interface. The complexity is even more pronounced for the waves generated near the minimum of the dispersion curve. If $V > V_c$, there are two values of k for which $V = c_p$ (see Fig. 1). Then, as can be seen from the dispersion law, Eq. (1) and Fig. 1, the waves with $k < \kappa$ have a group velocity $c_g = \partial\omega/\partial k$ smaller than $c_p = V$, i.e., the energy travels through a fluid faster than the stream. On the other hand, the waves with $k > \kappa$ have $c_g > c_p = V$, so that the energy travels upstream from the object. Thus, the short ripples are found upstream (in front of the object), and the long waves downstream (behind the object) from the object, respectively.

Figure 22 represents an image of the capillary-gravity water surface waves just above the transition. It provides complete information about the wave pattern and wavelength distribution. First, let us extract simple information about the opening angle of the Cherenkov cone and the wavelength along the direction of motion. The inset in Fig. 23 shows the dependence of the wave number of the capillary ripples on a water surface in front of the ball on the flow velocity together with the fit. The main plot presents the data for cos θ as a function of the velocity. Due to dispersion the phase velocity of the waves depends on the wave number. We used the fit of the wave numbers versus velocity from the inset in Fig. 23 to obtain the corresponding values of $c(k)$ in Eq. (3). The result of the calculations of cos θ according to Eq. (3) is shown by a solid line in Fig. 23. If one takes into account that no fitting parameters were used in this procedure, the
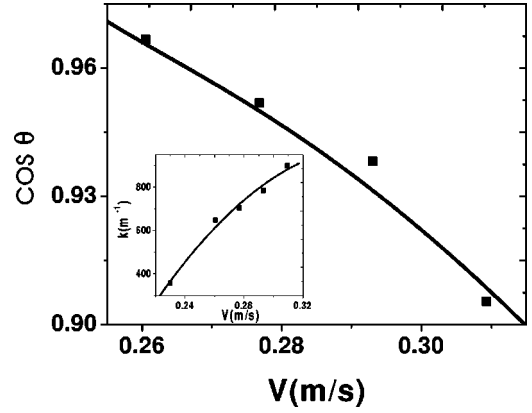
agreement with the data is rather surprising. Particularly, the critical velocity V_c, obtained from extrapolation of $\theta \rightarrow 0$, is sufficiently close to the value found from the force measurements.

A. Wave crests equations. Comparison with experiment

A more complete analysis of the capillary-gravity wave pattern and anisotropy of wave propagation requires an analytical derivation of a wave crests equations and their comparison with the experimentally observed images. It can be derived readily using the well-known techniques [2,3,19]. So we present just the final parametric equation for the wave crests shape, which is quantitatively compared with the digitized wave crests taken from the experiment:

$$\tan \alpha_{c,g}$$
$$= \frac{\sin\theta[1 + 3\kappa^{-2}k_{c,g}^2(\theta)]}{2V\sqrt{k/g[1 + \kappa^{-2} \cdot k_{c,g}^2(\theta)]} - \cos\theta[1 + 3\kappa^{-2}k_{c,g}^2(\theta)]},$$
(16)

where

$$k_g(\theta) = \kappa\left(\frac{V}{V_c}\right)^2 \{\cos^2\theta - [\cos^4\theta - \cos^4\chi]^{1/2}\}, \quad (17)$$

$$k_c(\theta) = \kappa\left(\frac{V}{V_c}\right)^2 \{\cos^2\theta + [\cos^4\theta - \cos^4\chi]^{1/2}\}, \quad (18)$$

with cos $\chi = V_c/V$, $0 \le \chi < \pi/2$. The angles θ and α are defined in Fig. 24. The result of the comparison of the theoretical expression for the wave crests and the experimental pattern for capillary-gravity waves, generated in water by a 3.14-mm-diameter ball, is shown in Fig. 25. Good quantitative agreement is clearly found.

VI. CONCLUSIONS

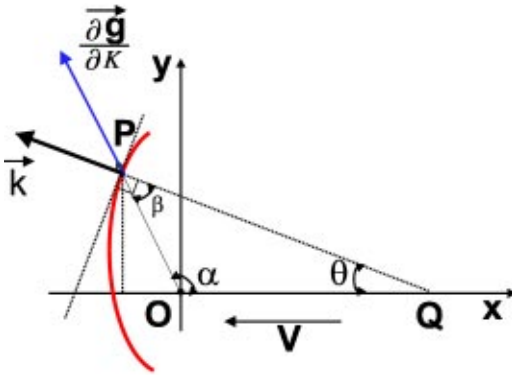The main goal of the experiments described in the paper is to characterize the transition from the no-wave to the

FIG. 24. Geometry of a wave crest.

FIG. 25. Experimental data on the wave crests generated in water by a 3.14-mm-diameter ball, squares; calculated wave crests, full lines.

wave-generating state in the case of the capillary-gravity surface waves. The experiment was conducted with a disturbing object of size d smaller than the capillary wave length λ_c, which is the intrinsic characteristic size in the system. Such an object generates the waves with the wavelength of the order of λ_c, as was expected and found in the experiment. The experiment was designed in a way to avoid variations in the capillary force due to relocation of the object due to applied force. The capillary force particularly for low viscosity fluids exceeds orders of magnitude the wave drag force near the onset, which is a subject of the study. Thus, any deviations of the object from an initial position lead to redistribution and alteration of the capillary force, and cause a significant error in the results on the wave resistance force. This statement was verified by the experiments.

As a result of the experiment the following was found. The idea [12] that the wave resistance shows up via the bifurcation is correct. However, in a strong contradiction with the theory [12] a continuous transition to the wave drag state is found. It is the main result of the experiment. The continuous bifurcation imposes a broken symmetry in a full hydrodynamic problem, where the corresponding order parameter is the reduced drag force. This theoretical problem requires an analysis of symmetries in the problem.
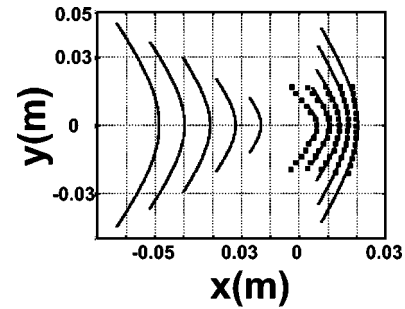
Based on our experimental observations, the scaling of the reduced wave drag force with the physical parameters and the ball size was suggested. We showed also that the scaling is compatible with the dimensional analysis. As a result of the scaling, all the data on the reduced wave drag force versus reduced velocity for various fluids and the ball sizes are collapsed on a single curve. The capillary-gravity wave pattern and the shape of the wave-generating region was investigated both experimentally and theoretically. Good agreement between the theory and the experimental data was found.

[1] L. D. Landau and E. M. Lifshitz, *Fluid Mechanics*, 2nd ed. (Pergamon Press, New York, 1987).

[2] J. Lighthill, *Waves in Fluids* (Cambridge University Press, Cambridge, 1996).

[3] H. Lamb, *Hydrodynamics*, 6th ed. (Cambridge University Press, Cambridge, 1993).

[4] Lord Kelvin, Proc. R. Soc. London, Ser. A **42**, 80 (1887).

[5] T. H. Havelock, *Collected Papers* (Office Naval Research, Washington D.C., 1966).

[6] A. A. Kostyukov, *Theory of Ship Waves and Wave Resistance* (Effective Commun., Iowa City, 1968).

[7] M. I. Shliomis and V. Steinberg, Phys. Rev. Lett. **79**, 4178 (1997).

[8] T. H. Havelock, Proc. R. Soc. London, Ser. A **84**, 197 (1910).

[9] P. A. Cherenkov, C. R. Acad. Sci. URSS **8**, 451 (1934); I. Frank and I. Tamm, *ibid.* **14**, 109 (1937).

[10] L. D. Landau and E. M. Lifshitz, *Statistical Physics*, 3rd ed. (Pergamon Press, New York, 1980), Pt. 2.

[11] Y. Pomeau and S. Rica, Phys. Rev. Lett. **71**, 247 (1993); Y. Pomeau, Int. J. Bifurcation Chaos Appl. Sci. Eng. **4**, 1165 (1994).

[12] E. Raphaël and P.-G. de Gennes, Phys. Rev. E **53**, 3448 (1996).

[13] D. Richard and E. Raphaël, Europhys. Lett. **48**, 53 (1999).

[14] Shu-Ming Sun and J. Keller, Phys. Fluids **13**, 2146 (2001).

[15] J. Browaeys, J.-C. Bacri, R. Perzynski, and M. Shliomis, Europhys. Lett. **53**, 209 (2001).

[16] T. Burghelea and V. Steinberg, Phys. Rev. Lett. **86**, 2557 (2001).

[17] J. D. Jackson, *Classical Electrodynamics* (Wiley, New York, 1987).

[18] We have found that the scaling with the ratio $\nu\sigma/d^2$ gives better results than the previously used ratio $\eta\sigma/d^2$ in Ref. [16]. We also corrected a misprint for the scaling made in Ref. [16].

[19] G. B. Whitham, *Linear and Nonlinear Waves* (Wiley, New York, 1974).